Check for updates

High electrostrictive properties and energy storage performances with excellent thermal stability in Nb-doped $Bi_{0.5}Na_{0.5}TiO_3$-based ceramics†

Yichen Wu, [ID][ab] Genshui Wang,[*bcd] Zheng Jiao,[a] Yuzhu Fan,[b] Ping Peng[b] and Xianlin Dong[bcd]

As a promising candidate material replacing $Pb(ZrTi)O_3$ (PZT), the lead-free $Bi_{0.5}Na_{0.5}TiO_3$ (BNT) system exhibits outstanding piezoelectric and ferroelectric properties. However, the weak thermal stability of these electric properties hampers its practical applications. In this work, we designed and prepared novel Nb-doped $0.76Bi_{0.5}Na_{0.5}TiO_3-0.24Bi_{0.5}K_{0.5}TiO_3$ (BNT–BKT) ceramics with superior temperature stability of electric properties. Both strain as well as discharging properties of 5% Nb-doped BNT–BKT ceramics varied less than 3% and 12.5% respectively from room temperature to 160 °C, ascribed to the enlarged gap between the depolarized temperature (T_d or T_{F-R}) and the maximum dielectric temperature (T_m). In addition, we investigated the impacts of Nb doping on the phase transition, dielectric, piezoelectric and ferroelectric behaviors of BNT–BKT ceramics in detail. Temperature dependent dielectric spectrums indicated that T_d decreased below room temperature with Nb modifying, revealing that the phase structure transformed from ferroelectric into ergodic relaxor. Accordingly, the maximum strain value of 0.21% and recoverable energy storage of 1.2 J cm^{-3} were simultaneously acquired at the critical composition of 5% Nb incorporation. Our results provide an effective means of obtaining BNT-based ceramics with simultaneously thermally stable strain and discharge properties for wide temperature actuator and capacitor applications.

1. Introduction

Over the past decades, lead-based ceramics such as $PbMg_{1/3}Nb_{2/3}O_3$-$PbTiO_3$ (PMN-PT), $Pb(ZrTi)O_3$ (PZT) systems were widely investigated in applications of various electromechanical devices owing to their preeminent electric properties.[1,2] However, taking into account the irreversible ecological harm caused by lead containing components, developing lead-free materials with alternative properties has inspired much efforts. In recent years, because of their high Curie temperature (320 °C) as well as large spontaneous polarization (~38 μm C^{-1}),[3] $Bi_{0.5}Na_{0.5}TiO_3$ (BNT) ceramics with superior electromechanical performances have received widespread attention. Nevertheless, the high loss and large coercive field (E_c) due to the

vaporization of the Bi element result in impaired electric properties of BNT-based ceramics, hampering their practical applications.[4]

A number of binary systems were designed to improve the electric performances of BNT ceramics, for instance, $Bi_{0.5}Na_{0.5}TiO_3$-$Bi_{0.5}K_{0.5}TiO_3$ (BNT–BKT), $Bi_{0.5}Na_{0.5}TiO_3$-$BaTiO_3$ (BNT–BT) and $Bi_{0.5}Na_{0.5}TiO_3$-$K_{0.5}Na_{0.5}NbO_3$ (BNT–KNN), *etc.*[5] Among these binary components, BNT–BKT systems demonstrate prominent piezoelectric performances with comprehensive superior electric field-induced strain (EFIS) and piezoelectric constant (d_{33}).[6] Especially, Tan *et al.*[7] obtained giant strain value of 0.7% in $((Bi_{1/2}(Na_{0.84}K_{0.16})_{1/2})_{0.96}Sr_{0.04})(Ti_{1-x}Nb_x)O_3$ ceramics at ambient temperature. Moreover, due to its intrinsic large saturated polarization, the BNT–BKT systems also provide great potential in the applications of energy storage fields.[8] Nevertheless, despite aforementioned competitive properties at room temperature, these performances will dramatically deteriorate when the temperature increases, unacceptable for realistic industrial applications and further restricting its development process. Up to now, the thermal stability of BNT-based ceramics is generally poor, and scarcely any attention has been focused on the weak thermal stability of them.[9]

For the past few years, several approaches had been done to improve the piezoelectric thermal stability of BNT-based ceramics through raising the depolarized temperature (T_d) to

aSchool of Environmental and Chemical Engineering, Shanghai University, Shanghai 200444, China

bKey Laboratory of Inorganic Functional Materials and Devices, Shanghai Institute of Ceramics, Chinese Academy of Sciences, Shanghai 200050, China. E-mail: genshuiwang@mail.sic.ac.cn

cThe State Key Lab of High Performance Ceramics and Superfine Microstructure, Shanghai Institute of Ceramics, Chinese Academy of Sciences, Shanghai 200050, China

dCenter of Materials Science and Optoelectronics Engineering, University of Chinese Academy of Sciences, Beijing 100049, China

† Electronic supplementary information (ESI) available. See DOI: 10.1039/c9ra04069b

a higher level to form an enlarged temperature range between RT and T_d, such as 0–3-type composites,[10] hot-pressed sintering (HPS),[11] and quenching process,[12] *etc.* The increased T_d improves the thermal stability of piezoelectricity and applies the BNT-based devices to high temperature accelerometers. With the rapid developments of actuators and capacitors recently, the requirements to enhance the thermal stability of strain and energy storage properties are also extremely urgent. Inspired by the strategy of raising the T_d to enhance the thermal stability of piezoelectricity mentioned above, lowering the T_d could enlarge the temperature range between T_d and T_m of strain performances and consequently contribute to the thermal stability of the strain properties. Lately, a great many studies demonstrated that Nb doping in BNT system could effectively break the long-range order, changing the nonergodic polar nanoregions (PNRs) into ergodic ones.[13] Furthermore, the addition of Nb would decrease the T_d below room temperature while maintain the maximum dielectric temperature (T_m), resulting to the extended temperature range between T_d and T_m.[14] In addition, a dielectric plateau would form with the increase of Nb content, conducive to the thermal stability of energy storage properties. Therefore, simultaneously thermally stable strain and energy storage behaviors are expected to be obtained in Nb-doped BNT-based ceramics.

In this work, novel Nb-doped 0.76BNT–0.24BKT binary solutions were prepared. The microstructure, dielectric, piezoelectric and ferroelectric properties were studied in detail. The maximum value of strain of 0.21% and energy storage density of 1.2 J cm^{-3} were simultaneously acquired at 5% doped BNT–BKT ceramics. To evaluate its thermal stability specifically, temperature-dependent strain and discharging properties were also investigated for actual application assessment. The results demonstrate that the strain and discharging properties vary below 3% and 12.5% respectively between 20 and 160 °C at 5% Nb doped BNT–BKT component, demonstrating its appropriate industrial applications in high temperature conditions.

2. Experimental procedure

The 0.76BNT-0.24BKT + xNb (x = 1%, 3%, 5%, 7%, abbreviated as 1Nb, 3Nb, 5Nb, 7Nb, respectively) ceramics were fabricated through solid-state reaction method. Weighed according to the stoichiometry, powders of reagent-grade Bi_2O_3 (99.99%), Na_2CO_3 (99.00%), TiO_2 (99.80%), K_2CO_3 (99.99%), Nb_2O_5 (99.38%) were mixed with agate media and anhydrous ethanol followed by ball-milling for 24 h. Subsequently, the powders were calcined at 850 °C in an air environment. The calcined powders needed ball-milling for 24 h one more time for the sake of the fine particle size. After that, the polyvinyl alcohol PVA was added as binder for granulation. Disks of 13 mm in diameter and 2 mm in thickness were prepared through uniaxial pressing under 150 MPa. After burning out the binder at 750 °C, the samples were sintered at 1150–1200 °C for 2 h in an air atmosphere. In order to avoid the volatile elements of Na, Bi and K, the ceramics were buried in the corresponding powders in the sintering process. For the purpose of electric measurements,

circular silver electrodes were coated on both sides of the polished samples.

X-ray diffraction (XRD, D/MAX-2550V; Rigaku, Tokyo, Japan) was utilized to analyze the phase structure of the ceramics. Micrographs of the polished and thermal etched surface was observed by scanning electron microscope (FESEM, Magellan400, FEI Company). Energy dispersive spectrometer (EDS) analysis was gathered from the attachment of the FESEM. The temperature dependence dielectric constant and tangent loss were tested by Hewlett Packard LCR meter. The polarization-electric hysteresis ($P–E$) loops, current-electric ($I–E$) loops as well as the strain curves are measured using a ferroelectric measurement system (aixACCT TF Analyzer 2000, Aachen, Germany). The charging–discharging properties were tested by a designed RC load circles.

3. Results and discussion

3.1 Phase formation and microstructure

Fig. 1a displays the XRD patterns of xNb ceramics at room temperature. As shown, the ceramics exhibit pure perovskite structure without any secondary phases when $x \leq 5\%$. However, with further increase of Nb content to x = 7%, the impurity phase $K_2Ti_6O_{13}$ (PDF#40-0403) is obviously observed as indexed in Fig. S1,† demonstrating the solid solution limit of 5%. Fig. 1b and (c) display the enlarged (111) and (200) peaks around 40°
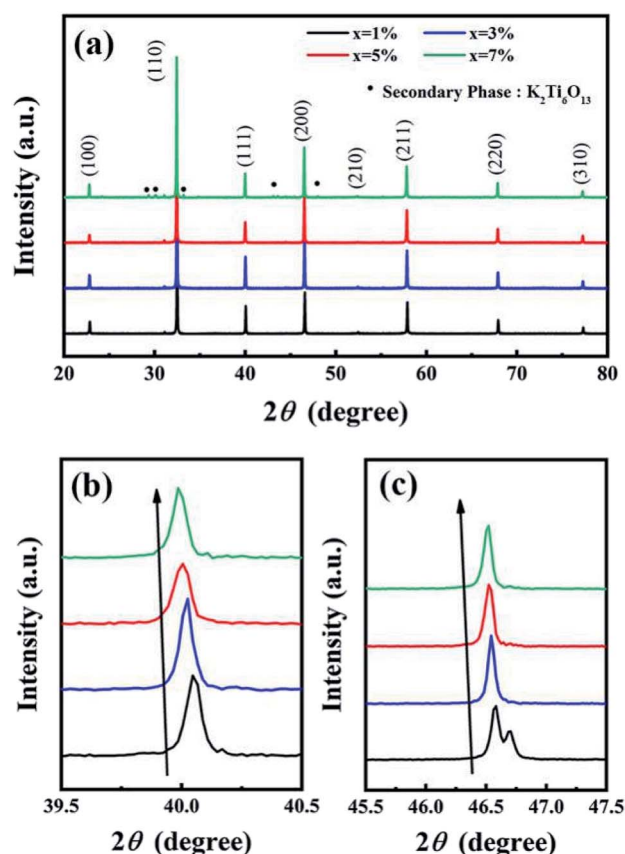

Fig. 1 (a) XRD patterns of xNb ceramics. (b and c) Enlarged (111) and (200) peaks around 40° and 46°, respectively.

and 46°, it can be observed that these two reflection peaks shift to lower angles, consistent with the larger Nb^{5+} ions replacing the Ti^{4+} ions with smaller radius [Ti^{4+}(0.604 Å, CN = 6), Nb^{5+}(0.64 Å, CN = 6)] at B-sites.[15] The phase structure of the ceramics transforms from $P4mm$ at 1Nb ceramics to pseudo-cubic structure with higher Nb content, evidenced from the fact that the (200)/(002) peaks merge into a single (200)$_{pc}$ peak.[16]

Fig. 2 display the SEM images of the polished and thermal-etched surface. The samples exhibit homogeneous and dense microstructures for compositions up to $x = 5\%$. The secondary phase obviously appears with the further increase of Nb content to $x = 7\%$. The results of the element spot scanning measured by EDS demonstrate that the secondary phase is Bi and Na deficient and K enriched phase, as shown in Fig. S2† and Table S1,† which is consistent with the K$_2$Ti$_6$O$_{13}$ phase determined by XRD. In addition, the average grain size doesn't display significant composition dependence with the similar average grain size ~2.3 μm measured through linear intercept method. The independence between composition and grain size indicates that the variation of strain and energy storage properties have no relation to the size of grain.

3.2 Dielectric properties

Fig. 3 presents the temperature dependence of dielectric constant (ε) and loss (tanδ) for poled ceramics under varied frequencies. Three significant dielectric abnormal peaks appear at T_{F-R}, T_s and T_m. The T_{F-R} (equal to the depolarized temperature T_d) reflects the ferroelectric to relaxor transition temperature, indicating that the ferroelectric $P4mm$ domains change into relaxor $P4bm$ polar nanodomains (PNRs) during heating. However, no T_{F-R} could be found in the dielectric curves when x

$\geq 3\%$, indicating that the T_{F-R} is below room temperature and the ceramics have changed into the relaxor phase with $p4bm$ nanodomains at room temperature.[17] The difference of phase structure obtained from XRD and ε–T curves is ascribed to the fact that the nanoscale structure could not detected by XRD accurately.[18] These nanodomains would grow into ferroelectric domains under electric field, conductive to large strain and energy storage properties. The T_s, which is related to the thermal evolution of tetragonal PNRs, also decreases with increase of the Nb content. It's noteworthy that the ε merges immediately as the temperature increase above T_s, revealing the disappearance of relaxor characteristics as well as the relation between T_s and the relaxor behavior in this system. With the temperature further increasing, the maximum dielectric constant ε_m appears at around 280 °C, which is usually defined as T_m (T_c). The barely changed T_m accompanied by notably decreased T_{F-R} results in the widened gap between T_{F-R} and T_m, as shown in Fig. 4. Furthermore, with the increasing Nb content, the dielectric constant maximum ε_m decreases sharply, getting closer to the dielectric constant value at T_s and resulting in the formation of dielectric plateau in a wide temperature range.[19] The temperature independence of the dielectric properties is closely related to the thermal stability of electric behaviors.[19]

3.3 Electrostrain properties

Fig. 5a exhibits the bipolar strain behaviors of xNb ceramics under 5 kV mm^{-1} and 10 Hz. The 1Nb ceramics exhibit typical butterfly-shaped bipolar S–E curves with a positive strain (S_{pos}) of 0.12% and negative strain (S_{neg}) of 0.1%, which is the characteristic of ferroelectrics as the negative strain is related to the
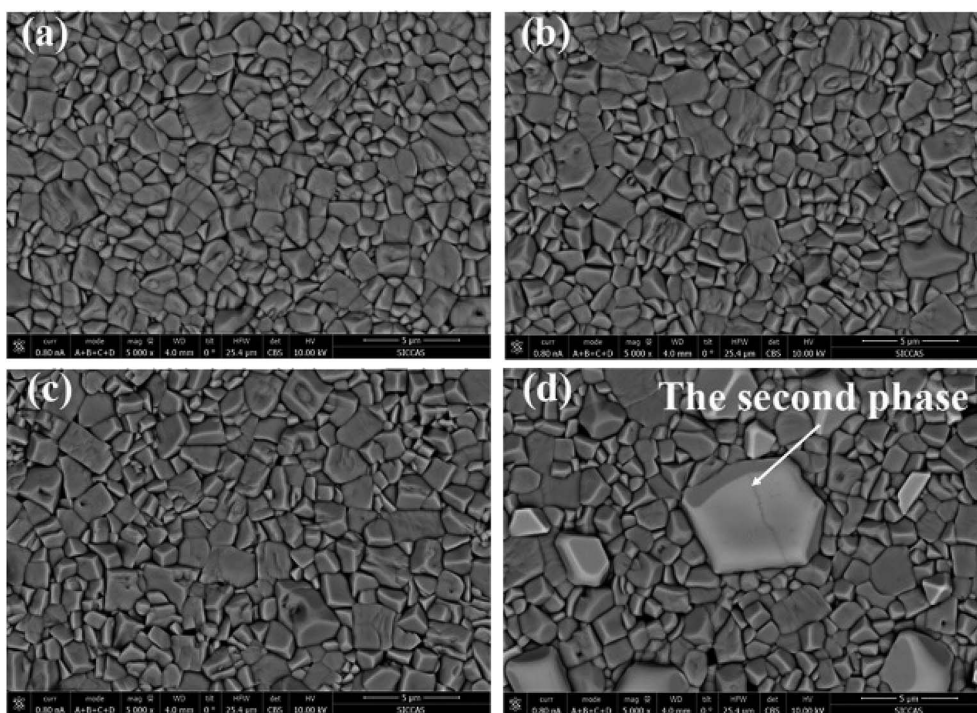

Fig. 2   The scanning electron microscopy photographs of xNb doped BNT−BKT ceramics with (a) $x = 1\%$, (b) $x = 3\%$, (c) $x = 5\%$, (d) $x = 7\%$.
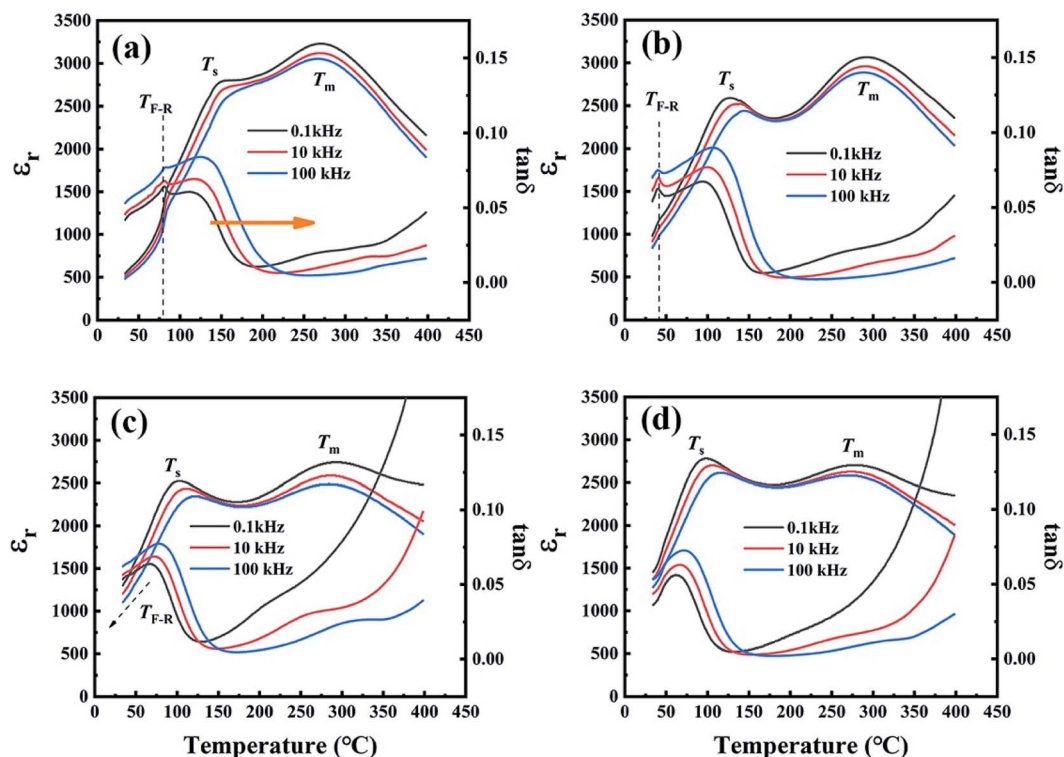
Fig. 3 Temperature dependent dielectric curves of xNb ceramics for (a) x = 1%, (b) x = 3%, (c) x = 5%, (d) x = 7% component.

domain back switching during loading electric field.[20] With the increase of Nb content, it could be clearly observed that the S_{neg} has been declining to 0 while the S_{pos} rises significantly. As illustrated in Fig. 5b, the S_{pos} and S_{neg} value reach the maximum of 0.19% and the minimum of 0 respectively at 5Nb ceramics. As the Nb content reaches 7%, the S_{pos} value drops to 0.12% and S_{neg} value remains 0. The decrease of S_{neg} is related to the reduction of the domain wall density induced by the Nb modifying, while the ultimate vanishment of which indicates that Nb-doped BNKT ceramics have changed into the ergodic relaxor ferroelectrics, in good agreement with dielectric curves.

Fig. 4 Phase diagram of xNb ceramics.

To assess the suitability of the designed ceramics in actuator applications, unipolar strain curves are depicted in Fig. 5c. On increasing the Nb content from 1% to 5%, the strain value increases from 0.10% to 0.21%, and decreases subsequently to 0.11% at x = 7%. To better explain the physical mechanism of the strain, the d_{33} as well as normalized strain S_{max}/E_{max} (d_{33}^*) of the xNb ceramics were measured and analyzed, as shown in Fig. 5d. The BNKT ceramics exhibit large d_{33} of 180 pC/N, in proximity with its d_{33}^* of 200 pm V^{-1}, indicating that the strain value of 1Nb ceramics mainly origins from the converse piezoelectric effect. With the increase of Nb doping, the d_{33} keeps reducing until nearly 0 pC/N at 7Nb ceramics while the d_{33}^* increases sharply reaching the maximum value of 420 pm V^{-1} at x = 5%, and eventually it reduces to 200 pm V^{-1} at x = 7%. This phenomenon reveals that the strain property mainly origins from the electric field induced relaxor and ferroelectric phase transition because of their low energy barrier.[21] The decrease of strain at x = 7% is caused by the enlarged energy barrier of the phase transition.

For the purpose of evaluating the thermal stability of the strain behavior, temperature dependent unipolar strain curves of the 5Nb component are characterized. As depicted in Fig. 6a, the 5Nb ceramics possess excellent thermal stability of the strain behavior, almost maintaining the fixed value in the measured temperature region of 20–160 °C with the variation less than 3%. The excellent thermal stability of this strain property is much superior than many other systems,[22–25] as displayed in Fig. 7. The excellent temperature independence of strain value of our 5Nb ceramics demonstrates its advantages in practical applications of actuators. Meanwhile, as shown in Fig. 6b, the strain hysteresis of these unipolar curves decreases
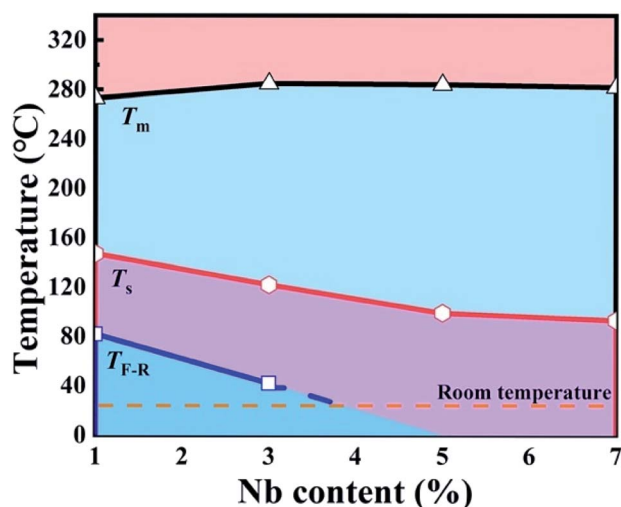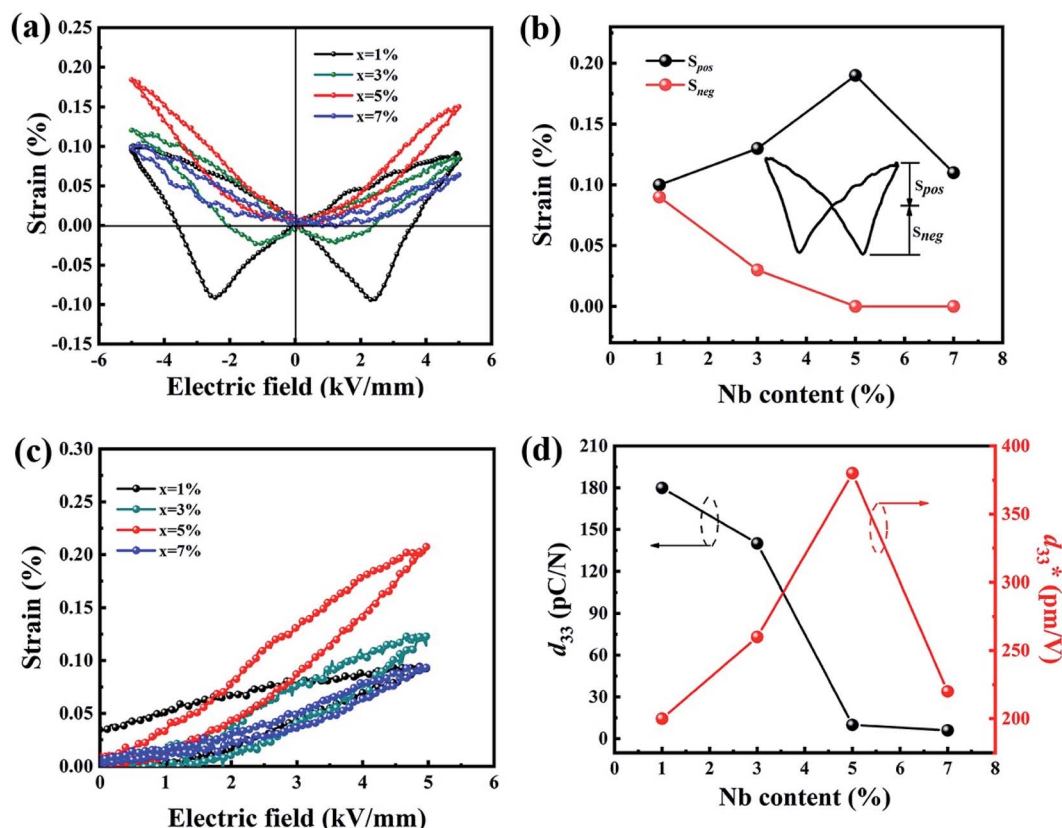
Fig. 5 The component dependent (a) bipolar strain and (c) unipolar strain curves of xNb ceramics under 5 kV mm^{-1}. (b) The evolution of component dependent S_{neg} and S_{pos}. (d) The component dependent piezoelectric constant d_{33} and normalized strain d_{33}^*.

sharply from 24% to 0 with the temperature increasing. It is worth noting that the strain value maintains a high level near T_s while the hysteresis is zero. This is an interesting phenomenon, because if the subsequent work can adjust the T_s to room temperature, the BNT-based ceramics with both high strain and ultra-low hysteresis can be obtained, which has great application prospects.

3.4 Energy storage properties

To characterize the energy storage performances of the ceramics, $P–E$ loops under critical electric field of 12 kV mm^{-1}

of different content of Nb are displayed in Fig. 8. The 1% Nb modified BNKT ceramics exhibit typical saturated ferroelectric performance with both large P_m and P_r of 48 μC cm^{-2} and 40 μC cm^{-2} respectively, corresponding to its butterfly-shaped strain curves. With the Nb content increasing to 5%, the P_r reduces dramatically accompanied by the decline of P_m, resulting in the pinched $P–E$ loops. The obvious changes of $P–E$ loops confirm that the long-range ferroelectric order of BNKT ceramics has been disrupted into ergodic relaxor (ER) phase.[26] As the Nb content further increases to 7%, the critical electric field for the phase transition between relaxor and ferroelectric increases
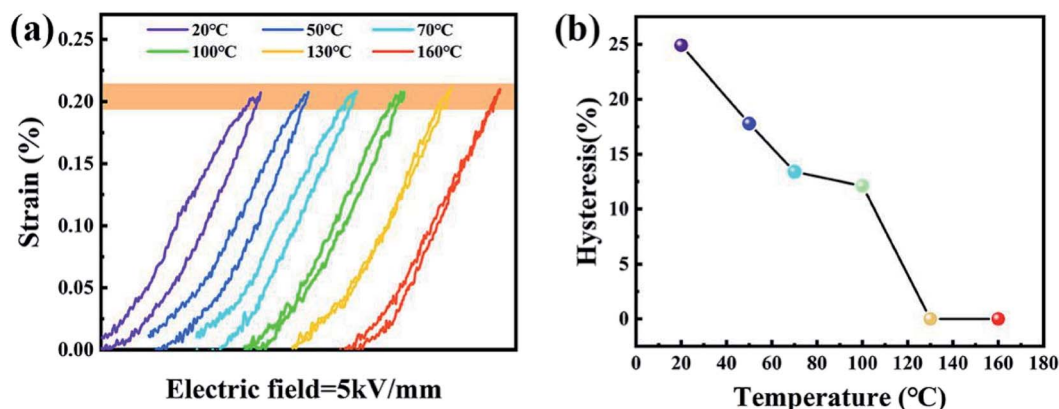

Fig. 6 The temperature dependent (a) the strain value of 5Nb ceramics and (b) the corresponding hysteresis.
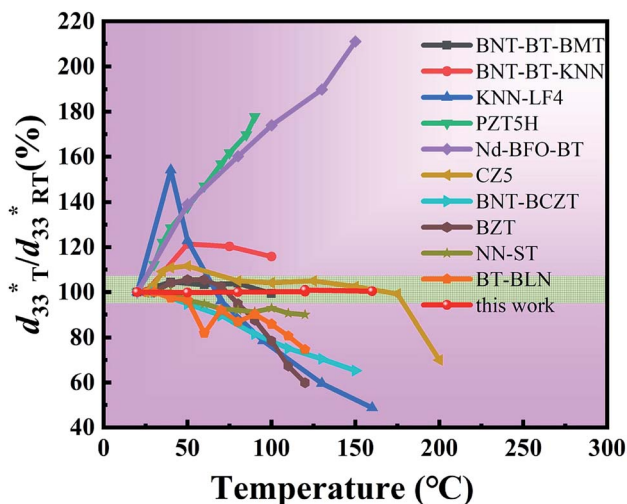
Fig. 7 Comparison of the temperature dependence of the d_{33}^* as normalized to the $d_{33,RT}^*$ for various systems.

sharply, evidenced by the quasi-linear loops with relatively low P_m. Fig. 8b presents the corresponding current-electric field (I–E) loops. As is displayed, the 1% doped BNKT ceramics show typical ferroelectric I–E curves with two sharp current switching peaks. The inherent ferroelectric order exists stably even when the electric field is withdrawn, manifested in the large P_r. On increasing the Nb content to 3%, four current peaks (P_1, P_2, P_3, P_4) appear,[6,26] it's reported that these four current peaks are

related to the ER phase induced by the Nb content modifying. The ER phase would transform into metastable ferroelectric phase under exerted electric field, corresponding to P_1/P_3 current peaks, resulting in large P_m. When removing the electric field, the induced long-range order would change back to the initial ER state, corresponding to P_2/P_4 current peaks, resulting in the low P_r. Both large P_m and low P_r are beneficial to acquire high energy storage property. According to the formula:[18,27,28]

$$\text{Energy storage density } (W) = \int_0^{P\text{max}} E dP \quad (1)$$

$$\text{Recoverable energy storage density } (W_{\text{rec}}) = \int_{Pr}^{P\text{max}} E dP \quad (2)$$

$$\text{Energy storage efficiency } (\eta) = (W)\frac{W\text{rec}}{W} \times 100\% \quad (3)$$

Where P, P_m, P_r, and E indicate the polarization, maximum polarization, remnant polarization, and exerted electric field, respectively. P_m and P_r play important role in improving the value of W_{rec}. Thus we summarized the P_m, P_r and ΔP ($P_m - P_r$) in Fig. 8c. When increasing Nb content from 1% to 7%, P_m smoothly decreases from 48 μC cm^{-2} to 27 μC cm^{-2} while P_r sharply reduces from 40 μC cm^{-2} to 3 μC cm^{-2}. As a result, the ΔP achieves the maximum value of 32 μC cm^{-2} at 5Nb ceramics, boosting high W_{rec} of 1.2 J cm^{-3} in this component, as shown in Fig. 8d. In addition, the η value keeps increasing until $x = 7\%$, ascribed to the reduced hysteresis of P–E loops.

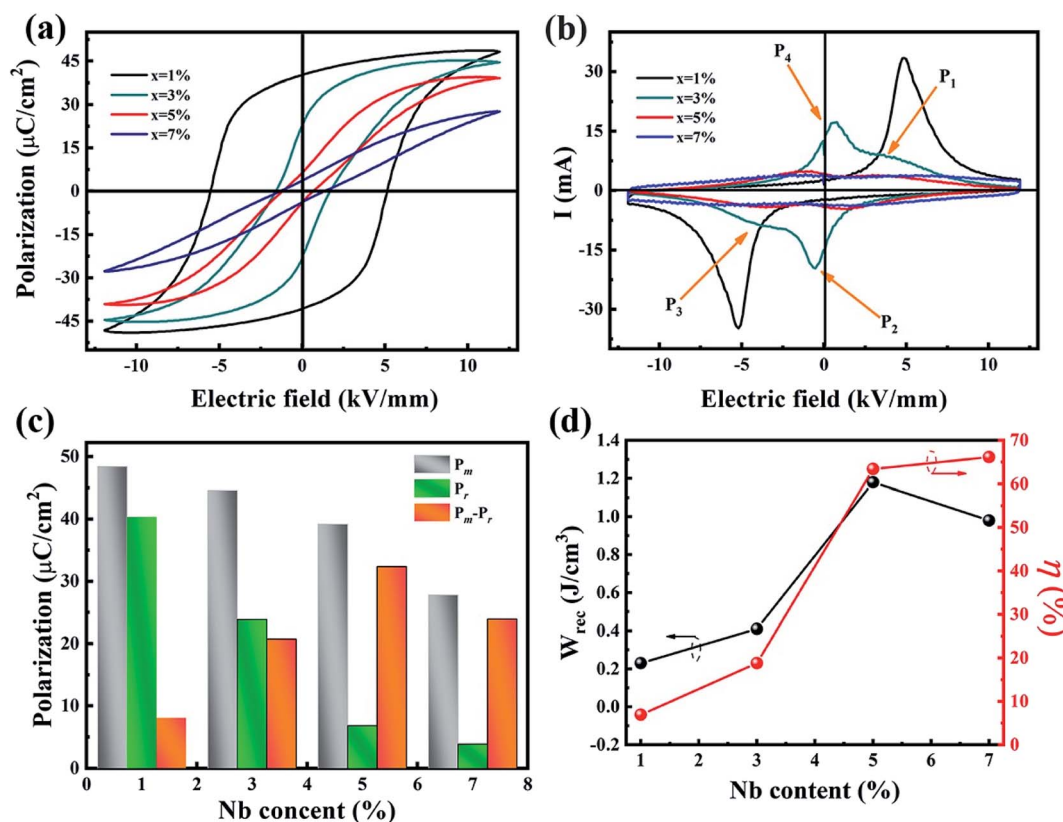**Fig. 8** (a) P–E loops of xNb ceramics and (b) corresponding I–E curves at room temperature. (c) The component dependent P_m, P_r and ΔP ($P_m - P_r$). (d) The component dependent calculated energy storage density and efficiency.
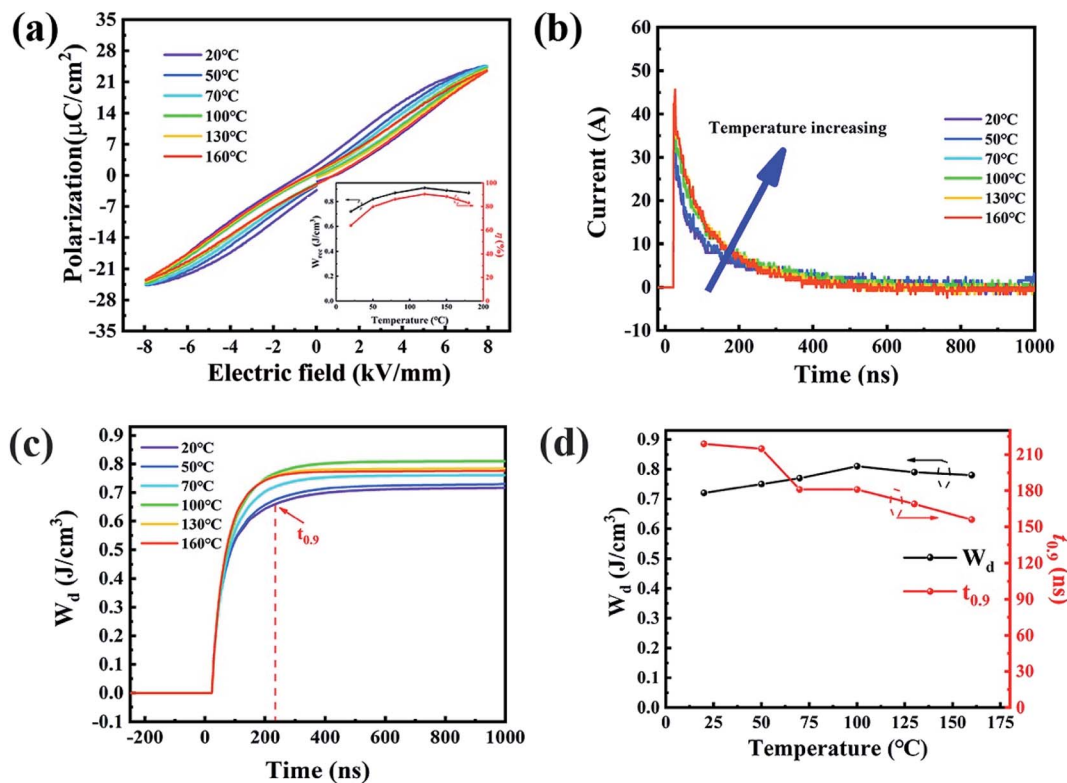
Fig. 9 (a) The temperature dependent P–E loops of 5Nb ceramics at 8 kV mm^{-1}, the inset shows corresponding W_{rec} and η. (b) Overdamped discharging current curves of the 5Nb ceramis at 8 kV mm^{-1}. (c) The calculated W_d–t curves. (d) The summarized W_d and $t_{0.9}$ values as a function of temperature.

3.5 Charging–discharging properties

To assess the temperature stability of the 5Nb ceramics, temperature dependent P–E loops at 8 kV mm^{-1} are depicted in Fig. 9a. The ferroelectric properties exhibit stable trend with the polarization value (P_m and P_r) exhibiting little changes in the measured temperature range from 20 to 160 °C, as displayed in the inset of Fig. 9a. To evaluate the practical application performances, temperature dependent overdamped discharge current curves of the 5Nb ceramics under 8 kV mm^{-1} are illustrated in Fig. 9b. As shown, the 5Nb ceramics exhibit similar discharging performances under different temperature, with the current curves reaching the maximum value rapidly and lasting less than 1 μs. In the measuring temperature range, the current curves maintain the peak value of 46 A, exhibiting

excellent thermal stability. According to the formula $W_d = R \int i(t)^2 \mathrm{d}t/V$, where the R, V denote the total load resistor (200 Ω) and sample volume respectively,[29] the calculated W_d–t value are illustrated in Fig. 9c. The $t_{0.9}$ indicated by the dash line in Fig. 9c means the time required to release 90% of the stored energy (W_d). It's noteworthy that the W_d and $t_{0.9}$ change from 0.72 J cm^{-3} and 124.8 ns to 0.81 J cm^{-3} and 121.6 ns respectively in the range of 20–160 °C, keeping the variation less than 12.5%, as illustrated in Fig. 9d. The superior thermal stability of the 5Nb ceramics demonstrates its great potential in high temperature energy storage applications.

At present, the doping of elements mainly improves the temperature stability of strain or energy storage performances singly, and there are fewer materials simultaneously possessing

Table 1 The temperature stability of the investigated materials compared with other perovskite systems[a]

Materials	Strain	Variation	W_{rec} (J cm^{-3})	Variation	Temperature range	References
Ho doped BCZT	~0.165%	<2%	—	—	20–70 °C	30
Sb doped KNN-SZ-BNZ	~0.14%	<10%	—	—	20–180 °C	31
Ta doped BNKT-ST	~0.35%	~46%	0.52	<10%	25–135 °C, 75–150 °C	32
BNT modified BT	—	—	2.14	<12%	25–175 °C	33
BFO modified BCT-BMT	—	—	0.39	~15%	25–110 °C	34
BZS modified BT	—	—	~1.12	<15%	20–160 °C	35
Nb doped BNT-BKT (this work)	**0.21%**	**<3%**	**1.2**	**<15%**	**25–160 °C**	**This work**

[a] PZT: Pb(Zr$_{0.53}$Ti$_{0.47}$)O$_3$ BCZT: (Ba$_{0.85}$Ca$_{0.15}$)(Zr$_{0.1}$Ti$_{0.9}$)O$_3$ KNN: (K$_{0.48}$Na$_{0.52}$)NbO$_3$ SZ: SrZrO$_3$ BNZ: (Bi$_{0.5}$Na$_{0.5}$)ZrO$_3$ BNKT: Bi$_{0.5}$(Na$_{0.84}$K$_{0.16}$)$_{0.5}$TiO$_3$ ST: SrTiO$_3$ BCT: Ba$_{0.8}$Ca$_{0.2}$TiO$_3$ BMT: BiMg$_{0.5}$Ti$_{0.5}$O$_3$ BZS:Bi(Zn$_{0.5}$Sn$_{0.5}$)O$_3$.

temperature and energy storage stability. Despite this, our Nb-doped BNT-based ceramics attained superior results in temperature stability in both strain and energy storage performances compared with other currently promising materials, as shown in Table 1.[30–35] Therefore, these results provide new strategies for the application researches of BNT-based ceramics.

4. Conclusion

In this work, we designed and prepared Nb modified BNT-based ceramics with excellent thermal stability through simple solid-state reaction method. Enhanced strain and energy storage properties (0.21% and 1.2 J cm^{-3} respectively) were obtained in 5Nb ceramics due to relaxor and ferroelectric phase transition. The extended temperature range between $T_{F–R}$ and T_m accompanied by wider dielectric plateau jointly contribute to the thermal stability of piezoelectric and discharging behaviors. As a result, the strain and discharge energy density of 5Nb component vary less than 3% and 12.5% respectively in the temperature range of RT and 160 °C. The excellent temperature stability of 5Nb ceramics indicates its outstanding applications in the high temperature conditions of dielectric capacitors and actuators.

Conflicts of interest

There are no conflicts of interest to declare.

Acknowledgements

References

1 J. Rödel, K. G. Webber, R. Dittmer, W. Jo, M. Kimura and D. Damjanovic, *J. Eur. Ceram. Soc.*, 2015, **35**, 1659–1681.

2 P. Baettig, C. F. Schelle, R. LeSar, U. V. Waghmare and N. A. Spaldin, *Chem. Mater.*, 2005, **17**, 1376–1380.

3 M. Davies, E. Aksel and J. L. Jones, *J. Am. Ceram. Soc.*, 2011, **94**, 1314–1316.

4 R. A. Malik, A. Hussain, A. Maqbool, A. Zaman, T. K. Song, W.-J. Kim and M.-H. Kim, *J. Alloy. Comp.*, 2016, **682**, 302–310.

5 G. Dong, H. Fan, J. Shi, M. Li and W. Jo, *J. Am. Ceram. Soc.*, 2015, **98**, 1150–1155.

6 X. Zhou, Z. Yan, H. Qi, L. Wang, S. Wang, Y. Wang, C. Jiang, H. Luo and D. Zhang, *J. Eur. Ceram. Soc.*, 2019, **39**, 2310–2317.

7 X. Liu and X. Tan, *Adv. Mater.*, 2016, **28**, 574–578.

8 Y. Wu, Y. Fan, N. Liu, P. Peng, M. Zhou, S. Yan, F. Cao, X. Dong and G. Wang, *J. Mater. Chem. C*, 2019, **7**, 6222–6230.

9 L. Jin, W. Luo, L. Wang, Y. Tian, Q. Hu, L. Hou, L. Zhang, X. Lu, H. Du, X. Wei, G. Liu and Y. Yan, *J. Eur. Ceram. Soc.*, 2019, **39**, 277–286.

10 J. Zhang, Z. Pan, F. F. Guo, W. C. Liu, H. Ning, Y. B. Chen, M. H. Lu, B. Yang, J. Chen, S. T. Zhang, X. Xing, J. Rodel, W. Cao and Y. F. Chen, *Nat. Commun.*, 2015, **6**, 6615.

11 R. I. Mahdi and W. H. A. Majid, *RSC Adv.*, 2016, **6**, 81296–81309.

12 Z.-T. Li, H. Liu, H.-C. Thong, Z. Xu, M.-H. Zhang, J. Yin, J.-F. Li, K. Wang and J. Chen, *Adv. Electron. Mater.*, 2019, **5**, 1800756.

13 K.-N. Pham, A. Hussain, C. W. Ahn, W. Kim, S. J. Jeong and J.-S. Lee, *Mater. Lett.*, 2010, **64**, 2219–2222.

14 L. Li, M. Zhu, Q. Wei, M. Zheng, Y. Hou and J. Hao, *J. Eur. Ceram. Soc.*, 2018, **38**, 1381–1388.

15 R. D. Shannon, *Acta Crystallogr.*, 1976, **A32**, 751–767.

16 F. Li, K. Yang, X. Liu, J. Zou, J. Zhai, B. Shen, P. Li, J. Shen, B. Liu, P. Chen, K. Zhao and H. Zeng, *Scripta Mater.*, 2017, **141**, 15–19.

17 J. Wu, A. Mahajan, L. Riekehr, H. Zhang, B. Yang, N. Meng, Z. Zhang and H. Yan, *Nano Energy*, 2018, **50**, 723–732.

18 W. Huang, Y. Chen, X. Li, G. Wang, N. Liu, S. Li, M. Zhou and X. Dong, *Appl. Phys. Lett.*, 2018, **113**, 203902.

19 F. Hu, X. Chen, P. Peng, F. Cao, X. Dong and G. Wang, *J. Am. Ceram. Soc.*, 2018, **101**, 4434–4440.

20 Z. Rashad and A. Feteira, *Mater. Lett.*, 2018, **222**, 180–182.

21 L. Wang, R. Liang, Z. Zhou and X. Dong, *Scripta Mater.*, 2019, **164**, 62–65.

22 J. Hao, W. Li, J. Zhai and H. Chen, *Mater. Sci. Eng., R*, 2019, **135**, 1–57.

23 L. Jin, J. Qiao, L. Wang, L. Hou, R. Jing, J. Pang, L. Zhang, X. Lu, X. Wei, G. Liu and Y. Yan, *J. Alloy. Comp.*, 2019, **784**, 931–938.

24 X. Lu, L. Hou, L. Jin, L. Wang, Y. Tian, K. Yu, Q. Hu, L. Zhang and X. Wei, *Ceram. Int.*, 2018, **44**, 5492–5499.

25 X. Lu, L. Wang, L. Jin, Q. Hu, Y. Tian, L. Hou, K. Yu, L. Zhang, X. Wei, Y. Yan and G. Liu, *J. Alloy. Comp.*, 2018, **753**, 558–565.

26 N. Liu, R. Liang, Z. Zhou and X. Dong, *J. Mater. Chem. C*, 2018, **6**, 10211–10217.

27 N. Sun, Y. Li, Q. Zhang and X. Hao, *J. Mater. Chem. C*, 2018, **6**, 10693–10703.

28 T. Li, X. Lou, X. Ke, S. Cheng, S. Mi, X. Wang, J. Shi, X. Liu, G. Dong, H. Fan, Y. Wang and X. Tan, *Acta Mater.*, 2017, **128**, 337–344.

29 F. Li, X. Hou, J. Wang, H. Zeng, B. Shen and J. Zhai, *J. Eur. Ceram. Soc.*, 2019, **39**, 2889–2898.

30 L. Wang, W. Bai, X. Zhao, F. Wen, L. Li, W. Wu, P. Zheng and J. Zhai, *J. Mater. Sci.: Mater. Electron.*, 2019, **30**, 9219–9230.

31 X. Lv, J. Wu, J. Zhu and D. Xiao, *Phys. Chem. Chem. Phys.*, 2018, **20**, 20149–20159.

32 R. A. Malik, A. Hussain, A. Maqbool, A. Zaman, T. K. Song, W.-J. Kim and M.-H. Kim, *J. Alloy. Comp.*, 2016, **682**, 302–310.

33 L. Chen, H. Wang, P. Zhao, C. Zhu, Z. Cai, Z. Cen, L. Li and X. Wang, *J. Am. Ceram. Soc.*, 2019, **102**, 4178–4187.

34 M. Xu, B. Peng, J. Zhu, L. Liu, W. Sun, G. J. T. Leighton, C. Shaw, N. Luo and Q. Zhang, *J. Alloy. Comp.*, 2019, **789**, 303–312.

35 M. Zhou, R. Liang, Z. Zhou and X. Dong, *J. Mater. Chem. C*, 2018, **6**, 8528–8537.